Theoretical framework for energy flux analysis of channels under drag control

Xi Chen [*]
Key Laboratory of Fluid Mechanics of Ministry of Education, Beihang University (Beijing University of Aeronautics and Astronautics), 100191 Beijing, People's Republic of China

Jie Yao and Fazle Hussain
Department of Mechanical Engineering, Texas Tech University, Lubbock, Texas 79409, USA

(Received 13 July 2020; accepted 17 December 2020; published 19 January 2021)

A framework for analyzing energy flux in turbulent channel flows is proposed which enables quantification of the drag reduction efficacy by different control methods. In contrast to the FIK [Fukagata, Iwamoto, and Kasagi, Phys. Fluids **14**, L73 (2002)] and the RD [Renard and Deck, J. Fluid Mech. **790**, 339 (2016)] identities, this framework expresses the skin friction coefficient in terms of the nondimensionalized dissipation rate and the work done by external excitation. We extend the energy-box analysis of Gatti *et al.* [J. Fluid Mech. **857**, 345 (2018)] through a triple decomposition of energy flux and show how mean (ϵ_M), coherent (ϵ_C), and random turbulent (ϵ_R) dissipations contribute differently to the drag reduction and the net power saving. Three control methods, including our recently developed spanwise opposed wall-jet forcing (SOJF), the spanwise wall oscillation (SWO), and the opposed wall blowing/suction (OBS) controls, are compared at $\mathrm{Re}_\tau \approx 200$ via direct numerical simulations (DNS). While all methods yield comparable drag reductions (∼20%), OBS yields the maximum net power saving, followed by SOJF, and then SWO. Specifically, for SOJF control, ϵ_C (induced by the large-scale swirls) is much smaller than ϵ_R (induced mainly by the small-scale near-wall vortices) and ϵ_M (due to the spanwise vorticity sheet Ω_z). In contrast, for SWO control, ϵ_C (caused by the wall oscillation-induced Ω_x vortex sheet)—much larger than that of SOJF—is comparable to ϵ_R and ϵ_M. For OBS control, ϵ_R is notably suppressed without any introduction of ϵ_C as the energy is injected through the random velocity field. Diagnoses performed at a higher Re_τ (i.e., 2000) for SWO shows that random turbulent dissipation ϵ_R predominates due to the increasing near-wall vortical structures—hence their suppression should be the target for drag control at high Re_τ. The analysis also suggests a promising hybrid drag control strategy by incorporating both the random (OBS) and coherent (SOJF or SWO) controls together, an issue for future exploration.

DOI: 10.1103/PhysRevFluids.6.013902

I. INTRODUCTION

Reducing the drag of turbulent flows is of great importance for energy saving and pollution control. The basic idea for almost all drag control techniques is to suppress the regeneration of the near-wall streamwise vortices, which are the main contributors to turbulence production and drag generation [1–4]. However, random distributions and complex spatiotemporal dynamics of these vortices present formidable challenges for drag control strategies [5]. Active control methods,

[*]Corresponding author: chenxi97@outlook.com

such as spanwise wall oscillation (SWO) [6–10], opposite wall blowing/suction (OBS) [11–14], and spanwise opposite wall-jet forcing (SOJF) [15], have been proposed and examined via laboratory and numerical experiments. These studies showing notable drag reductions at moderate Reynolds numbers (Re) have promoted studies of effective controls at practically high Re [16].

In addition to demonstrating the possibility of achieving drag reductions, an important objective of drag control research is to understand its mechanism [16]. Previous works (e.g., Refs. [7,9,15,17,18]) have shown that drag reduction mainly results from the suppression of instability, mostly transient growth of the near-wall, low-speed streaks so that fewer streamwise vortices (SVs) are generated. Yet, the relationship between the SVs and drag at the wall is fairly qualitative. To better understand the mechanism as well as compare efficacies among different control methods, a unified quantitative framework is needed. Some statistical approaches which connect the drag with certain flow quantities have been proposed, such as the Fukagata-Iwamoto-Kasagi (FIK) identity [19] or later the Renard-Deck (RD) identity [20]. These identities are summarized here for comparison with ours for analyzing drag reduction.

Obtained through the wall-normal (y) integration of the streamwise mean momentum equation, the FIK identity for a channel flow reads

$$\frac{C_f}{2} = \frac{3}{\mathrm{Re}_b} + 3\int_0^1 \frac{(1-y')\overline{-u'v'}}{u_b^2}dy', \tag{1}$$

where C_f is the skin friction (or drag) coefficient, and $\mathrm{Re}_b = u_b H/\nu$ is the bulk Reynolds number with u_b being the bulk velocity, H the half-channel height, ν the kinematic viscosity, and $\overline{-u'v'}$ the Reynolds shear stress. When Re_b is kept constant by setting a constant flow rate (not constant pressure gradient or power input as investigated by Ref. [21]), the drag is reflected solely by the Reynolds shear stress. Further decomposition, such as separating the small and large scales for channels [15,22] or turbulent boundary layers [23], or the inner and outer regions [24,25], can be introduced for $\overline{-u'v'}$ in Eq. (1) to independently evaluate the contributions. In Ref. [26], scale separation has been applied to analyze the drag contribution by the large-scale outer structures in channels under spanwise wall oscillations.

However, Renard and Deck [20] commented that the FIK identity lacks information on energy dynamics and proposed an alternative expression for drag coefficient (hereafter referred to as the RD identity), i.e.,

$$\frac{C_f}{2} = \int_0^1 \frac{\epsilon_M}{\epsilon_*}dy' + \int_0^1 \frac{\overline{-u'v'}\partial_y\overline{u}}{\epsilon_*}dy'. \tag{2}$$

Here, ϵ_M $(=\nu\partial_y\overline{u}\partial_y\overline{u})$ is the dissipation of mean flow (shown later); $\overline{-u'v'}\partial_y\overline{u}$ is turbulent production and $\epsilon_* = u_b^3/H$ is a characteristic dissipation rate defined by the bulk velocity and the half-channel height. Compared to the FIK identity, the RD identity illustrates how turbulent production contributes to drag. On the other hand, in the RD identity, mean shear $\partial_y\overline{u}$ contributes to both mean dissipation and production rates, quantifying C_f mainly by the mean flow strain rate. For a straightforward connection between vortical structures and drag coefficient, it might be more proper to investigate turbulent dissipation, an important quantity for understanding turbulent flows (see Vassilicos [27]) and closely related with coherent structures.

In this paper, we aim to present an energy flux paradigm which leads to a uniform diagnosis of different control methods. The framework builds on a general identity which quantifies the drag via the volume integrated dissipation and the work done by external forcing, i.e.,

$$\frac{C_f}{2} = \int_0^1 \frac{\epsilon_M}{\epsilon_*}dy' + \int_0^1 \frac{\epsilon_f}{\epsilon_*}dy' - \frac{W}{\epsilon_*}. \tag{3}$$

Compared to the RD identity, Eq. (3) replaces the production by turbulent dissipation ϵ_f and the power spent by the control W (which may include energy transport for spatially developing flows), which enables a direct estimation of net power saving. Scale separation or inner-outer decomposition also can be introduced for turbulent dissipation ϵ_f in Eq. (3), which could be used to examine the Re effect of drag reduction. Note that for flows without control, $W = 0$ and Eq. (3) has been obtained by Laadhari [28] and Abe and Antonia [29] for analyzing the Reynolds number scaling of the mean flow. Here, we are interested in the energy flux under control. On the other hand, Gatti *et al.* [21] recently introduced an extended Reynolds decomposition of total dissipation where the mean velocity is split into a laminar component and a deviation from it. They further analyzed the Re dependence of the energy flux and the increased flow rate by controls (and hence drag reduction under constant power input) through an integration of the Reynolds shear stress profile. Different from Gatti *et al.* [21], we introduce a triple-decomposed budget analysis [30] on Eq. (3) to illustrate how controls of mean, coherent, and turbulent flow structures contribute differently to the drag reduction and the net power saving rate. Through the decomposition, active control strategies can be classified into random (e.g., OBS) or coherent controls (e.g., SWO and SOJF), depending on how control energy is injected to the flow. The analysis also suggests that a hybrid control may be developed by injecting energy into both random and coherent motions, a topic for future exploration.

Several points are notable for Eq. (3). First, as dissipation is induced by viscous strain of fluids at the smallest (Kolmogorov) scale, Eq. (3) seems to emphasize more small-scale turbulence compared to large scales by the FIK and RD identities. However, there is no indication that small-scale control should be dominant over large-scale control, taking into account that the source of ϵ_R is large-scale production. In other words, suppressing large-scale turbulence would intercept the energy cascade process, leading to smaller ϵ_R and hence drag reduction. Thus, Eq. (3) has no indication on which scale to operate for the optimal drag control. Moreover, it is the integration of dissipation over the entire flow domain rather than any local dissipation that determines the drag coefficient. Therefore, turbulent dissipation ϵ_R taking its maximum at about $y^+ = 15$ does not mean that turbulence near the walls is dominant than other flow regimes for drag control, while the integration of ϵ_R in the logarithmic layer is the leading contributor to C_f [31]. This is the same for the FIK and RD identities, all showing dominant integrations from the log layer than from other regions. Finally, Eq. (3) replaces only the Reynolds shear stress in Eq. (1) or production in Eq. (2) by dissipation and power input, and no further complication is involved. However, the triple decomposition of energy flux introduced below requires a more detailed analysis and interpretation. Such a careful analysis is helpful when one uses turbulence models (e.g., the k-ϵ model) to predict drag reduction at much higher Re, as the current results may help to calibrate the parameters and to develop advanced assumptions for better agreement with energy dynamics, and hence more convincing modeling predictions.

The paper is organized as follows. Section II presents the theoretical part including our drag coefficient expression and the triple decomposition of the energy budget. In Sec. III, a case-by-case study for the drag reduction at $\mathrm{Re}_\tau \approx 200$ is performed for SOJF, SWO, and OBS controls. Physical structures and higher Re_τ results are addressed in Sec. IV. Finally, conclusions are given in Sec. V.

II. ANALYSIS FRAMEWORK FROM BALANCE EQUATIONS

A. Identity for friction coefficient

The Navier-Stokes equations for an incompressible turbulent channel flow are (density ρ absorbed in the pressure p)

$$\partial u_i/\partial x_i = 0, \tag{4}$$

$$\partial_t u_i + \partial_j u_i u_j = \nu \partial_j \partial_j u_i - \partial_i p + F_i. \tag{5}$$

Here, x_i for index $i = 1, 2, 3$ indicates streamwise x, wall-normal y, and spanwise z directions, and u, v, w denote the velocities in each of the directions, respectively (a double index indicates summation). F_i represents the external force in the x_i direction (e.g., for the SOJF control, only $F_z \neq 0$ so that the force acts only in the spanwise direction).

The total kinetic energy equation obtained by multiplying Eq. (5) with u_i is

$$\partial_t \frac{u_i u_i}{2} + \partial_j \frac{u_i u_i u_j}{2} = \nu \partial_j \partial_j \frac{u_i u_i}{2} - \nu \partial_j u_i \partial_j u_i - \partial_i (p u_i) + u_i F_i. \tag{6}$$

Averaging the above equation over time period (T) of control and the flow volume ($L_x \times 2H \times L_z$), i.e.,

$$\langle \phi \rangle_{t,x,y,z} = \int_0^T \int_0^{L_x} \int_0^{L_z} \int_0^{2H} \frac{\phi}{2H L_x L_z T} dydxdzdt, \tag{7}$$

yields

$$\langle \epsilon \rangle = \nu \langle \partial_j \partial_j (u_i u_i) \rangle / 2 + \langle -\partial_j (u_i u_i u_j) \rangle / 2 + \langle -u_i \partial_i p \rangle + \langle u_i F_i \rangle, \tag{8}$$

which describes the energy balance between the dissipation $\langle \epsilon \rangle \equiv \nu \langle \partial_j u_i \partial_j u_i \rangle$, diffusion $\nu \langle \partial_j \partial_j (u_i u_i) \rangle / 2$, transport $-\langle \partial_j u_i u_i u_j \rangle / 2$, work done by pressure $\langle -\partial_i (p u_i) \rangle$, and the external force $\langle u_i F_i \rangle$. Here, for simplification, $\langle \phi \rangle_i$ indicates ensemble average with respect to the index i, while $\langle \phi \rangle = \langle \phi \rangle_{t,x,y,z}$ for short.

Explicit expressions of each term on the right-hand side of Eq. (8) are given through integration by parts as follows. For diffusion, it is actually

$$D_w \equiv \nu \langle \partial_j \partial_j (u_i u_i) \rangle / 2 = \langle -\nu \partial_y (u_i u_i)|_{y=0} \rangle_{t,x,z} / 2H = \langle -\nu u_i \partial_y u_i|_{y=0} \rangle_{t,x,z} / H = \langle -u_{i,w} S_{gn} u_{i,\tau}^2 \rangle / H, \tag{9}$$

where S_{gn} indicates the sign of the derivative $\partial_y u_i|_{y=0}$; $u_{i,\tau} = \sqrt{|\nu \partial_y u_i|_{y=0}|}$ represents the friction velocity u_τ, v_τ, and w_τ, and $u_{i,w}$ represents wall velocity u_w, v_w, w_w for $i = 1, 2, 3$, respectively. Clearly, both w_w and w_τ are nonzero for SWO, indicating energy input through the wall diffusion process. For the control of body forcing such as SOJF or OBS, the energy input from diffusion D_w is zero.

For spatial transport in Eq. (8), it is zero if $v_w = 0$ but injects a power of $\langle v_w u_{i,w} u_{i,w} \rangle / 2$ to the flow under OBS, i.e.,

$$J_{w1} \equiv \langle -\partial_j (u_i u_i u_j) \rangle / 2 = \langle v_w u_{i,w} u_{i,w} \rangle / 2H. \tag{10}$$

In fact, the blowing/suction effect also has a power input through a pressure correlation. This is because

$$\langle -u_i \partial_i p \rangle = \langle -\partial_i (p u_i) \rangle = \langle -\partial_y (p v) \rangle + \langle -\partial_x (p u) \rangle, \tag{11}$$

where the p-v correlation term is

$$J_{w2} \equiv \langle -\partial_y (p v) \rangle = \langle p_w v_w \rangle / H, \tag{12}$$

again resulting from the blowing/suction.

The p-u correlation term in Eq. (11) is $\langle -\partial_x (p u) \rangle = -u_b \langle \partial_x p \rangle$, representing the power injected by the mean pressure gradient along the streamwise direction. Moreover, $\langle \partial_x p \rangle$ can be estimated by applying the time and volume average on the streamwise momentum equation in Eq. (5), which, for the case of $F_1 = 0$, yields

$$-\langle \partial_x p \rangle = \langle \partial_y (u v) \rangle - \nu \langle \partial_y \partial_y u \rangle = -\langle u_w v_w \rangle / H + \langle u_\tau^2 \rangle / H. \tag{13}$$

For flows subject to $\langle u_w v_w \rangle = 0$, the pumping power is $P = \langle -\partial_x (p u) \rangle = u_b \langle u_\tau^2 \rangle / H$, balancing the energy consumption by the viscous drag at the wall, while for $\langle u_w v_w \rangle \neq 0$, they are different.

Substituting the estimations Eqs. (9)–(13) into Eq. (8) yields a general expression for energy balance where SOJF, SWO, and OBS are all present,

$$\langle \epsilon \rangle = D_w + J_w + u_b \langle u_\tau^2 \rangle / H + \langle u_i F_i \rangle, \tag{14}$$

where the net energy input due to OBS reads

$$J_w = J_{w1} + J_{w2} - u_b \langle u_w v_w \rangle / H = \langle v_w u_{i,w} u_{i,w} \rangle / 2H + \langle p_w v_w \rangle / H - u_b \langle u_w v_w \rangle / H. \tag{15}$$

Replacing the u_τ^2 term in Eq. (14) by the definition of friction coefficient $C_f/2 = \langle u_\tau^2\rangle/u_b^2$ yields

$$\frac{C_f}{2} = \frac{1}{\epsilon_*}(\langle\epsilon\rangle - \langle u_i F_i\rangle - D_w - J_w), \tag{16}$$

where $\epsilon_* = u_b^3/H$. The above relation indicates a simple balance among the energy spent by working against the drag force, the energy dissipated by the viscous fluid, and the power inputs through control strategies. Moreover, introducing the Reynolds decomposition $\phi = \overline{\phi} + \phi'$, where the overbar indicates $t - x - z$ averaging, i.e., $\overline{\phi} = \langle\phi\rangle_{t,x,z}$, and ϕ' the Reynolds-decomposed fluctuation, then

$$\overline{\epsilon} = \epsilon_M + \epsilon_f, \tag{17}$$

with the mean dissipation $\epsilon_M = \nu\partial_y\overline{u}\partial_y\overline{u}$ and turbulent dissipation $\epsilon_f = \nu\overline{\partial_j u_i'\partial_j u_i'}$. Substituting Eq. (17) into Eq. (16) yields Eq. (3) with

$$W = \langle u_i F_i\rangle + D_w + J_w. \tag{18}$$

For flows without control, D_w, J_w, and $\langle u_i F_i\rangle$ are all zero, and Eq. (3) is equivalent to the RD identity as the balance between the integral of turbulent dissipation $\overline{\epsilon}_f$ and production $P_M = \overline{-u'v'}\partial_y\overline{u}$. Furthermore, considering the wall-normal integrated streamwise mean momentum equation deduced from Eq. (5), i.e.,

$$\nu\partial_y\overline{u} - \overline{u'v'} = \langle u_\tau^2\rangle(1 - y/H), \tag{19}$$

one obtains the FIK identity after replacing the mean shear in Eq. (3) or (2) by the Reynolds shear stress in Eq. (19). Nevertheless, for flows with control, for example, when both u_w and v_w are nonzero (corresponding to a hybrid control with both streamwise oscillation and blowing/suction), Eq. (19) is no longer valid due to a nonzero $\langle u_w v_w\rangle$ in the mean pressure gradient according to Eq. (13). As a consequence, certain modifications are needed for the FIK identity as well as for the RD identity under controls, such as to include an additional term $\langle u_w v_w\rangle/u_b^2$; however, Eq. (3) is general.

B. Triple-decomposed energy flux

Applying the Reynolds decomposition to the total kinetic energy in Eq. (6), we obtain the balance equations of ϵ_M and ϵ_f, i.e.,

$$\partial_t\frac{\overline{u}_i\overline{u}_i}{2} + \partial_j\left(\frac{\overline{u}_i\overline{u}_i\overline{u}_j}{2} + \overline{u}_i\overline{u_i'u_j'}\right) = \nu\partial_j\partial_j\frac{\overline{u}_i\overline{u}_i}{2} - \epsilon_M - \partial_i\overline{u}_i\overline{p} + \overline{u}_i\overline{F}_i + \overline{u_i'u_j'}\partial_j\overline{u}_i, \tag{20}$$

$$\partial_t\frac{\overline{u_i'u_i'}}{2} + \partial_j\left(\frac{\overline{u_i'u_i'u_j'}}{2} + \overline{u}_j\frac{\overline{u_i'u_i'}}{2}\right) = \nu\partial_j\partial_j\frac{\overline{u_i'u_i'}}{2} - \epsilon_f - \partial_i\overline{u_i'p'} - \overline{u_i'F_i'} - \overline{u_j'u_i'}\partial_j\overline{u}_i. \tag{21}$$

The volume integrated energy flux of mean and turbulent kinetic energy budgets is conceptually shown in Fig. 1(a).

Recently, Gatti *et al.* [21] have developed an extended energy flux analysis by decomposing the mean flow into the equivalent laminar and remnant parts. Differing with Gatti *et al.* [21], here we present a triple decomposition of energy flux composed of mean, coherent, and random turbulent parts. Following Reynolds and Hussain [32], the triple decomposition is introduced as

$$u_i = \overline{u}_i + \tilde{u}_i + u'', \quad \tilde{u}_i = \langle u_i\rangle_{x\alpha} - \overline{u}_i, \quad u_i'' = u_i' - \tilde{u}_i, \tag{22}$$

where α indicates time t (and z-periodicity) averaging for SOJF, while spanwise z (and t-periodicity) averaging for SWO; $\tilde{u}_i$ is the coherent part, and u_i'' is the random turbulence part, satisfying $\overline{\tilde{u}}_i = 0$, $\overline{u_i''} = 0$, and $\widetilde{u_i''} = 0$. Accordingly, the turbulent dissipation is decomposed to coherent and random

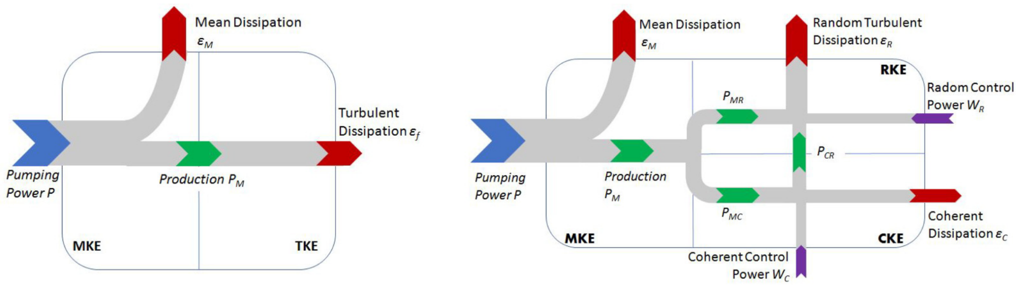

(a) (b)

FIG. 1. Sketch of energy flux box in channel by (a) Reynolds decomposition and (b) triple decomposition. Note that all the symbols have been time and volume averaged (the brackets $\langle\ \rangle$ have been omitted). Abbreviations MKE, TKE, CKE, and RKE represent mean, turbulent, coherent, and random kinetic energies, respectively. Drag reduction is indicated by the saving of pumping power P, while the net power saving by the additional subtraction of control power W $(= W_c + W_R)$.

fluctuation parts, i.e.,

$$\underbrace{\nu\overline{\partial_i u'_j \partial_i u'_j}}_{\epsilon_f} = \underbrace{\nu\overline{\partial_i \tilde{u}_j \partial_i \tilde{u}_j}}_{\epsilon_C} + \underbrace{\nu\overline{\partial_i u''_j \partial_i u''_j}}_{\epsilon_R}. \tag{23}$$

The triple-decomposed energy equations are obtained from Eq. (21) after a few lines of algebra, which, for the coherent part, is

$$\partial_t \frac{\overline{\tilde{u}_i\tilde{u}_i}}{2} + \partial_j\left(\frac{\overline{\tilde{u}_j\tilde{u}_i\tilde{u}_i}}{2} + \overline{\tilde{u}_i\widetilde{u''_i u''_j}} + \bar{u}_j\frac{\overline{\tilde{u}_i\tilde{u}_i}}{2} + \overline{\tilde{u}_j\tilde{p}}\right) = \nu\Delta\frac{\overline{\tilde{u}_i\tilde{u}_i}}{2} - \epsilon_C + \overline{\tilde{u}_i\tilde{F}_i} - \overline{\tilde{u}_i\tilde{u}_j}\partial_j\bar{u}_i + \overline{\widetilde{u''_i u''_j}\partial_j\tilde{u}_i}, \tag{24}$$

while for the random turbulent fluctuation part is

$$\partial_t \frac{\overline{u''_i u''_i}}{2} + \partial_j\left(\frac{\overline{u''_i u''_i u''_j}}{2} + \frac{\overline{\tilde{u}_j\widetilde{u''_i u''_i}}}{2} + \bar{u}_j\frac{\overline{u''_i u''_i}}{2} + \overline{u''_j p''}\right)$$
$$= \nu\Delta\frac{\overline{u''_i u''_i}}{2} - \epsilon_R + \overline{u''_i F''_i} - \overline{u''_i u''_j}\partial_j\bar{u}_i - \overline{\widetilde{u''_i u''_j}\partial_j\tilde{u}_i}. \tag{25}$$

Compared to the Reynolds-decomposed energy equation, it is interesting to note that the production splits into two parts, one coherent, and the other random fluctuation, i.e.,

$$\underbrace{-\overline{u'_j u'_i}\partial_j\overline{u_i}}_{P_M} = \underbrace{-\overline{\tilde{u}_i\tilde{u}_j}\partial_j\bar{u}_i}_{P_{MC}} + \underbrace{-\overline{u''_i u''_j}\partial_j\bar{u}_i}_{P_{MR}}. \tag{26}$$

Also, there is a new term $P_{CR} = -\overline{\widetilde{u''_i u''_j}\partial_j\tilde{u}_i}$ in both Eqs. (24) and (25), which transfers energy from the coherent part to the random part.

After time and volume integration, Eqs. (20), (24), and (25) lead to

$$\langle\epsilon_M\rangle = P - \langle P_M\rangle, \tag{27a}$$
$$\langle\epsilon_C\rangle = \langle P_{MC}\rangle - \langle P_{CR}\rangle + \langle W_C\rangle, \tag{27b}$$
$$\langle\epsilon_R\rangle = \langle P_{MR}\rangle + \langle P_{CR}\rangle + \langle W_R\rangle, \tag{27c}$$

which represent the balance between dissipation of mean flow $\langle\epsilon_M\rangle$, pumping power $P = \langle-\partial_i\overline{u_i p}\rangle = -u_b\langle\partial_x p\rangle$, and mean production $\langle P_M\rangle$ for Eq. (27a); the balance between coherent dissipation $\langle\epsilon_C\rangle$, production from mean $\langle P_{MC}\rangle$, production to the random turbulent $\langle P_{CR}\rangle$, and

TABLE I. Details of the numerical discretization employed for the present simulations.

Control	Re_τ	Re_b	$L_x/h, L_z/h$	$N_x \times N_y \times N_z$
SOJF	200	3180	$4\pi, 2\pi$	$192 \times 129 \times 126$
WO	200	3180	$4\pi, 2\pi$	$256 \times 128 \times 256$
OBS	200	3180	$2\pi, \pi$	$128 \times 128 \times 128$
WO	2000	43478	$4\pi, 2\pi$	$2048 \times 768 \times 2048$

control power to coherent motion $\langle W_C\rangle$ for Eq. (27b); and the balance between the random turbulent dissipation $\langle\epsilon_R\rangle$, production from mean $\langle P_{MR}\rangle$, production from coherent $\langle P_{CR}\rangle$, and control power from random motion $\langle W_R\rangle$ for Eq. (27c). Through the above decomposition, the energy box of mean turbulent is now extended to the triple-energy flux shown in Fig. 1(b). It is clear that without control, production from mean flow is balanced by turbulent dissipation, while under control, both coherent and random turbulent parts receive energy from mean production, and there is also an energy flux from the coherent to random part. Expressions of power input from coherent (W_C) and random (W_R) motions are shown case by case in the subsequent section.

C. Drag reduction and net power saving

Through the above analysis of energy flux, the rates of drag reduction and net power saving can be estimated straightforwardly. For uncontrolled flow, pumping power balances the total dissipation, i.e., $P_0 = \epsilon_0 = \langle u_{\tau,0}^2\rangle u_b/H$ (here, subscript 0 indicates uncontrolled). With these denotations, the drag reduction rate is

$$\mathcal{R} \equiv (C_{f,0} - C_f)/C_{f,0} = 1 - \langle u_\tau^2\rangle/\langle u_{\tau,0}^2\rangle = 1 - \langle\epsilon\rangle/P_0 + \langle u_i F_i\rangle/(HP_0) + D_w/(HP_0) + J_w/(HP_0), \tag{28}$$

where Eq. (16) has been substituted. For flows with $\langle u_w v_w\rangle = 0$ so that $P = u_b\langle u_\tau^2\rangle/H$ from Eq. (13), Eq. (28) is simply

$$\mathcal{R} \equiv (C_{f,0} - C_f)/C_{f,0} = 1 - \langle u_\tau^2\rangle/\langle u_{\tau,0}^2\rangle = 1 - P/P_0. \tag{29}$$

Furthermore, the net power saving rate is

$$\mathcal{N} \equiv (P_0 - P - W)/P_0 = 1 - \langle\epsilon\rangle/P_0. \tag{30}$$

As $P_0 = \epsilon_o = \langle\epsilon_{M,0}\rangle + \langle\epsilon_{f,0}\rangle = \langle\epsilon_{M,0}\rangle + \langle\epsilon_{R,0}\rangle$ (since $\epsilon_{C,0} = 0$), Eq. (30) is rewritten as

$$\mathcal{N} = 1 - \langle\epsilon\rangle/P_0 = \underbrace{(\langle\epsilon_{M,0}\rangle - \langle\epsilon_M\rangle)/P_0}_{\mathcal{N}_M} + \underbrace{(\langle\epsilon_{R,0}\rangle - \langle\epsilon_R\rangle)/P_0}_{\mathcal{N}_R} \underbrace{-(\langle\epsilon_C\rangle)/P_0}_{\mathcal{N}_C}, \tag{31}$$

where $\mathcal{N}_M, \mathcal{N}_R, \mathcal{N}_C$ are mean, random, and coherent contributions to net power saving, respectively. Hence,

$$\mathcal{R} = \underbrace{\mathcal{N}_M + \mathcal{N}_R + \mathcal{N}_C}_{\mathcal{N}} + \underbrace{\langle u_i F_i\rangle/(HP_0) + D_w/(HP_0) + J_w/(HP_0)}_{\mathcal{N}_{\mathrm{in}}}, \tag{32}$$

which indicates that the drag reduction rate $\mathcal{R}$ is a sum of net power saving rate $\mathcal{N}$ and the power input rate $\mathcal{N}_{\mathrm{in}}$. Below, a case-by-case examination of drag reduction for different controls is done using the above energy flux approach.

III. DRAG REDUCTION FOR DIFFERENT CONTROL METHODS

We present several direct numerical simulation (DNS) data sets of turbulent channel flow for these control methods [10,15] (the simulation parameters are listed in Table I). In the simulations, a constant flow rate is set and the bulk velocity u_b is maintained at a constant value by a control procedure that adjusts the mean pressure gradient. Periodicity in the streamwise and spanwise directions is imposed, and the no-slip and no-penetration conditions are applied at the walls. The simulations for SOJF control are based on the open-source finite-difference software INCOMPACT3D [33,34]. For the spatial derivatives, sixth-order compact schemes are used on a Cartesian grid stretched in the wall-normal direction. The time integration is performed using a low-storage third-order Runge-Kutta scheme. The SWO and OBS cases are performed with the highly parallelized pseudospectral code of Lee and Moser [35]. The incompressible Navier-Stokes equations are solved using the method of Kim *et al.* [36], in which equations for the wall-normal vorticity and the Laplacian of the wall-normal velocity are time advanced. This formulation has the advantage of satisfying the continuity constraint exactly while eliminating the pressure. A Fourier-Galerkin method is used in the streamwise and spanwise directions, while the wall-normal direction is represented using a seventh-order *B*-spline collocation method. A low-storage implicit-explicit scheme based on third-order Runge-Kutta for the nonlinear terms and Crank-Nicolson for the viscous terms are used for time advance.

A. Opposite wall blowing/suction control

The opposite wall blowing/suction control was first proposed by Choi *et al.* [11], where approximately 25% drag reduction was achieved in turbulence channel flow at $\mathrm{Re}_\tau \approx 110$ with the detection plane located at $y_d^+ = 10$. Hammond *et al.* [37] later studied the effect of the detection location y_d^+ and found that the maximum drag reduction is reached when $y_d^+ = 15$. They also showed that for the drag reduction case, the OBS establishes a virtual wall halfway between the detection plane and the wall, where approximately no flow passes through, thus inhibiting the momentum transfer in the wall-normal direction. Chung and Talha [12] systematically investigated the effects of the detection plane y_d^+ and amplitude A, and found that a substantial drag reduction is achieved for $20 < y_d^+ < 30$ if $A^+ < 1$. Consistent with Ref. [37], maximum drag reduction was achieved with $A^+ = 1$ and $y_d^+ = 15$. In addition, they showed that the maximum drag reduction for different y_d^+ is always obtained with the root mean square (rms) of the wall blowing/suction velocity $v_w'^+ = 0.25$. Deng and Xu [13] examined the effect of OBS on the generation of the near-wall streamwise vortices by resorting to the streak transient growth (STG) mechanism [18]. Inspired by this work, they further proposed a strengthened out-of-phase OBS, and a maximum drag reduction rate of about 33% was achieved [4]. Based on the similarity of the wall-normal velocity fluctuation and the Reynolds shear stress of the controlled flows with the uncontrolled case, they also proposed a formulation for the prediction of the drag reduction and disclosed that the location and the residual Reynolds shear stress of the virtual wall are the key factors in determining the drag reduction amount. Xia *et al.* [38] studied the OBS in the spatially developing turbulent boundary layer, and found that 22% drag reduction is obtained after the transient region. Stroh *et al.* [39] performed a comparison of OBS between the turbulent channel and boundary layer flows, and showed that, in spite of the very similar drag reduction rates that are achieved in both flows, the underlying drag reduction mechanisms are quite different.

For OBS control, the velocity at the wall is designated as

$$u_w = w_w = 0, \quad v_w(t,x,z) = -v_w(t,y_c,x,z), \tag{33}$$

where y_c indicates a specific height away from the bottom and top walls, respectively, and here chosen as $y^+ = 15$—the optimal value for $\mathrm{Re}_\tau = 200$ according to previous studies [37]. Under OBS control, the energy is injected into the flow through the random turbulence velocity. Hence, different from SOJF or SWO controls, there is no coherent part—all the coherent terms in the above triple decomposition are zeros. Thus, the balance equations of ϵ_M and ϵ_R (or ϵ_f) are

$$\epsilon_M = \underbrace{\nu\partial_y\partial_y(\overline{u}\overline{u})/2}_{D_M} \underbrace{-\partial_y(\overline{u}\overline{u'v'})}_{S_{TM}} + \underbrace{\overline{u'v'}\partial_y\overline{u}}_{-P_{MR}} \underbrace{-\overline{u}\partial_x\overline{p}}_{\text{Pump}}, \tag{34}$$

$$\epsilon_R = \underbrace{\nu\partial_y\partial_y\overline{u_i'u_i'}/2}_{D_R} \underbrace{-\partial_y\left(\overline{u_i'u_i'v'}/2 + \overline{v'p'}\right)}_{S_{TR}} \underbrace{-\overline{u'v'}\partial_y\overline{u}}_{P_{MR}}. \tag{35}$$

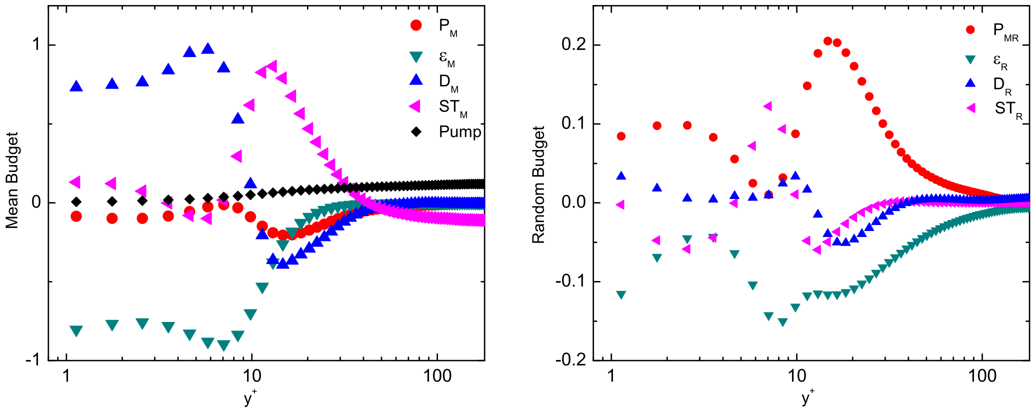

(a) (b)

FIG. 2. Energy budget at $\mathrm{Re}_\tau = 200$ under OBS control. (a) Mean kinetic energy and (b) turbulent fluctuation kinetic energy. Here, we take dissipation as negative to balance other terms.

The budgets for the mean kinetic energy and the fluctuation kinetic energy at $\mathrm{Re}_\tau = 200$ are shown in Fig. 2. Note the dominant balance between diffusion and dissipation for a mean budget near the wall ($y^+ < 10$). In contrast, for a random budget, the spatial transport induced by the blowing effect changes the sign from negative to positive at $y^+ \approx 5$ and exhibits a peak at $y^+ \approx 8$, causing a complex balance among all the processes of production, dissipation, spatial transport, and diffusion. Such a complicated balance becomes pellucid after volume averaging for the budget equations. The resulting energy flux in Fig. 3 clearly shows the following: (1) There is 23% (= 100%–77%) drag reduction as indicated by the pumping power saving; (2) while the mean dissipation decreases modestly by 8% (from 59% to 51%), turbulent dissipation is suppressed notably by 14% (from 41% to 27%), so that a 22% (= 8% + 14%) net power saving comes from Eq. (30) or (31); (3) the input power through random control W_R is 1%, consistent with the reduction of pumping power and the net power saving; and (4) turbulent production induced by the mean shear is reduced by 15% (from 41% to 26%) and is all converted to dissipation of random fluctuations, hence no flux in the coherent energy box. Note that hereinafter all the percentages are obtained by normalization using the pumping power of flow without control.

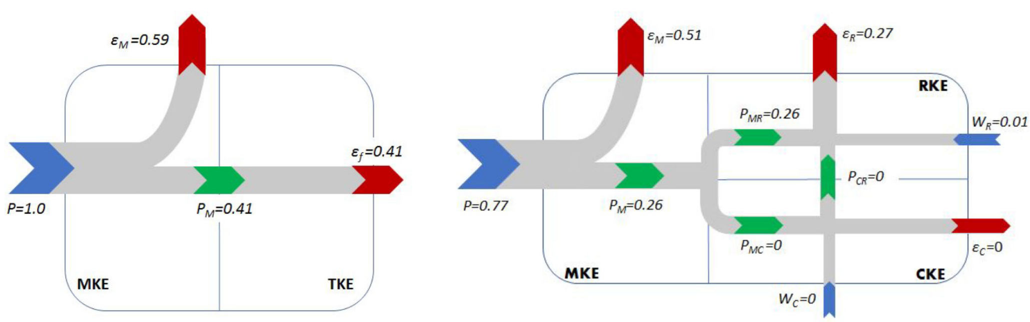

(a) (b)

FIG. 3. Energy flux in a channel at $\mathrm{Re}_\tau = 200$ (a) without control and (b) under OBS control. All the numbers are normalized by the pumping power of flow without control. Note that the drag reduction is 23% (indicated by the pumping power saving) and the net power saving is 22% (after a subtraction of control power).

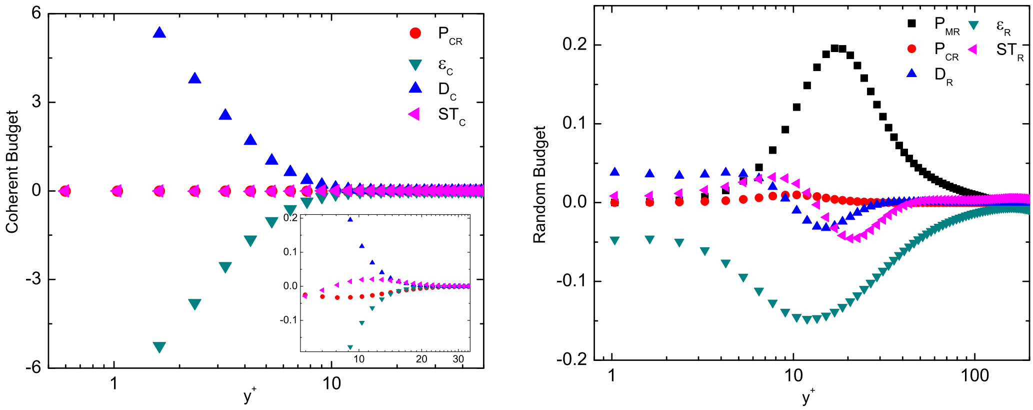

(a) (b)

FIG. 4. Energy budget at $\mathrm{Re}_\tau = 200$ for (a) coherent kinetic energy and (b) random fluctuation kinetic energy under SWO control. The inset of (a) is a zoom-in plot of the coherent kinetic energy budget.

B. Spanwise wall oscillation control

For spanwise wall oscillation, the velocity at the wall is given as

$$w_w(t) = A\sin(\omega t), \tag{36}$$

where A is the magnitude of SWO velocity, and $\omega = 2\pi/T$ is the frequency of oscillation with T the time period. SWO was first studied by Jung *et al.* [6] in a turbulent channel flow using DNS. This study revealed the sensitive dependence of the drag reduction on the oscillation frequency and demonstrated that an oscillation period $T^+ \equiv Tu_\tau^2/\nu$ of the order of 10^2 leads to a substantial decrease in the Reynolds stresses and the strength of the near-wall streak, causing as high as 40% drag reduction at $\mathrm{Re}_\tau = 200$. (Note that the superscript + indicates nondimensionalization by the wall variables of the uncontrolled flow.) Inspired by this work, a number of studies have been performed for channel [7–9,40,41], pipe [42,43], and boundary layers [44–47], as well as for duct flow [48] recently. In the case studied here, $A^+ \equiv A/u_\tau = 8$ and $T^+ = 100$.

According to the aforementioned triple decomposition, the coherent and random kinetic budget equations for SWO are

$$\epsilon_C = \underbrace{\nu\partial_y\partial_y\frac{\overline{\tilde{u}_i\tilde{u}_i}}{2}}_{D_C}\underbrace{-\partial_y(\overline{\tilde{v}\tilde{u}_i\tilde{u}_i}/2 + \overline{\tilde{u}_i\widetilde{u_i''v''}} + \overline{\tilde{v}\tilde{p}})}_{S_{TC}}\underbrace{-\overline{\tilde{u}\tilde{v}}\partial_y\bar{u}}_{P_{MC}} + \underbrace{\overline{\widetilde{u_i''v''}\partial_y\tilde{u}_i}}_{-P_{CR}}, \tag{37a}$$

$$\epsilon_R = \underbrace{\nu\partial_y\partial_y\frac{\overline{u_i''u_i''}}{2}}_{D_R}\underbrace{-\partial_y(\overline{u_i''u_i''v''}/2 + \overline{\tilde{v}\widetilde{u_i''u_i''}}/2 + \overline{v''p''})}_{S_{TR}}\underbrace{-\overline{u''v''}\partial_y\bar{u}}_{P_{MR}}\underbrace{-\overline{\widetilde{u_i''v''}\partial_y\tilde{u}_i}}_{P_{CR}}. \tag{37b}$$

Note that $\partial_z\tilde{\phi} = \partial_x\tilde{\phi} = 0$ for SWO. Moreover, since $\tilde{v} = 0$, the coherent budget of Eq. (37a) is simplified to

$$\epsilon_C = \underbrace{\nu\partial_y\partial_y\frac{\overline{\tilde{u}\tilde{u}} + \overline{\tilde{w}\tilde{w}}}{2}}_{D_C}\underbrace{-\partial_y(\overline{\tilde{u}\widetilde{u''v''}} + \overline{\tilde{w}\widetilde{w''v''}})}_{S_{TC}} + \underbrace{\overline{\widetilde{u''v''}\partial_y\tilde{u}} + \overline{\widetilde{w''v''}\partial_y\tilde{w}}}_{-P_{CR}}, \tag{38}$$

which indicates no production from the mean to the coherent part, the same as for control.

Figure 4(a) shows the budget of the coherent kinetic energy distribution at the same $\mathrm{Re}_\tau = 200$ under SWO. The prominent feature is that dissipation and diffusion are the two dominant terms

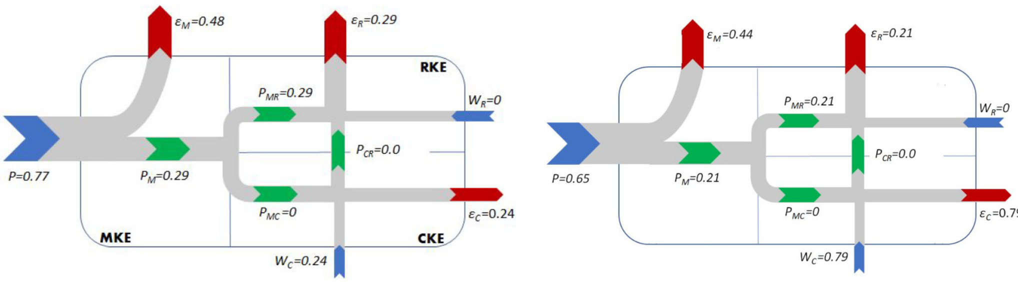

(a) (b)

FIG. 5. Energy flux in a channel at $\mathrm{Re}_\tau = 200$ under SWO control with (a) $A^+ = 8$ and (b) $A^+ = 12$.

balancing each other near the wall, indicating the control power is injected through the viscous diffusion, particularly, via the coherent motion, i.e., $\langle W_C\rangle = D_w = \langle w_w w_\tau^2\rangle$. The inset in Fig. 4(a) shows that spatial transport and production are at the same order of dissipation and diffusion only for $y^+ > 20$. In fact, the large diffusion and dissipation near the wall is due to the Stokes layer generated by SWO. According to the Stokes layer approximation of the spanwise momentum equation, i.e.,

$$\partial_t w \approx \nu \partial_y \partial_y w, \tag{39}$$

it has the analytical solution $w(y,t) = Ae^{-\eta}\cos(\omega t - \eta)$, where $\eta = y\sqrt{\omega/2\nu}$ (the laminar Stokes layer thickness is $\delta^+ = \sqrt{4\pi T^+}$ in wall units, which is $\delta^+ = 35.4$ for the current case of $T^+ = 100$). With such a solution, we can estimate the coherent diffusion (normalized by the pumping power P_0 at $\mathrm{Re}_\tau = 200$) $D_w = \nu\langle \partial_y\partial_y \tilde{w}^2/2\rangle \approx 0.80$, which is very close to the value of 0.79 obtained by numerical integration. Similarly, for dissipation, the estimation based on the laminar Stokes layer solution is $\epsilon_C = \nu\langle \partial_y \tilde{w}\partial_y \tilde{w}\rangle \approx 0.80$, again very close to the value 0.79 based on the DNS result. The congruence suggests that, instead of the spanwise vorticity sheet (i.e., $\partial_y \tilde{u}$), the streamwise vorticity sheet (i.e., $\partial_y \tilde{w}$) is the dominant contribution to coherent diffusion and dissipation effects.

The random turbulent kinetic energy budget under SWO is shown in Fig. 4(b). The turbulent production due to random fluctuations exceeds the diffusion to balance dissipation at $y^+ \approx 5$, while the production from the coherent part is negligible across the entire flow due to small $\partial_y \tilde{u}$ and $\widetilde{w''v''}$. Compared to control, all the budget terms near the wall behave smoothly, resembling closely the budget of turbulent kinetic energy for no control. Nevertheless, while dissipation takes its maximum at the wall for uncontrolled flow, it exhibits a maximum at $y^+ \approx 10$ and decreases as it approaches the wall under SWO. Such a decrease is reasonable, as random turbulence is significantly suppressed so that a well-characterized laminarlike Stokes layer is induced.

Figure 5(a) shows the integrated energy flux at $\mathrm{Re}_\tau = 200$ under SWO with $A^+ = 8$. Again, there is 23% drag reduction as indicated by the 23% saving of pumping power. In addition, the mean dissipation, turbulent random dissipation, and mean production are all similar to those under control. Such a coincidence is quite interesting as it indicates that the mean velocity field is similar between the flows under different controls. However, in contrast to OBS, $\langle W_R\rangle = 0$ for SWO control, as the control energy here is injected through the coherent motion of wall oscillation. As a result, the coherent dissipation increases, balancing the power input via wall oscillation. It is seemingly surprising that there is negligible energy flux from coherent to random, indicating that the coherent and random velocity fields are almost decoupled. The reason is that the coherent follows closely the laminarlike Stokes layer and barely interacts with the random turbulence fluctuation. According to Eq. (31), as the control power $\langle W_C\rangle = 24\%$ is much higher than that of OBS, the net power saving for this case is negative, i.e., $1 - (\epsilon_M - \epsilon_R - \epsilon_C)/P_0 = -1\%$. Note that the oscillation velocity effect of A is also examined for SWO control. Compared to 23% drag reduction by $A^+ = 8$ at $\mathrm{Re}_\tau = 200$, a larger $A^+ = 12$ yields a higher (35%) drag reduction at the same Re_τ [Fig. 5(b)], as both mean and random dissipations are suppressed more. However, the input power is increased by 55%, resulting in a negative power savings due to higher-energy consumption by coherent dissipation. Such a comparison implies that a better control of the coherent flow field is needed for net power saving, which is the goal of our large-scale control method (SOJF) addressed below.

C. Spanwise opposite wall-jet forcing control

To seek large-scale active control methods, which are robust and independent of instantaneous flow dynamics, in Yao *et al.* [15,49] we introduced a spanwise opposite wall-jet forcing method,

$$F_x = F_y = 0, \quad F_z = A\sin(\beta z)g(y^+), \tag{40}$$

where A is the forcing amplitude, β ($\Lambda = 2\pi/\beta$) is the spanwise wave number (wavelength), and $g(y^+)$ is a function scaling with the viscous unit y^+. Physically, the SOJF induces a pair of counter-rotating large-scale swirls, which can merge near-wall streaks and suppress the generation of streamwise vortices due to a reduced streak flank slope and cause drag reduction. Following previous works by Refs. [50–52], such a forcing is introduced to approximate the drag reduction strategy by Refs. [16,53,54], where spanwise velocity perturbations are induced by plasma actuators. For the function g, we choose the same form of the streak perturbation used in Ref. [18] for the transient instability growth, $g(y^+) = y^+\exp(-\eta y^{+2})$, where the decay factor η is chosen to specify the wall-jet velocity profile. The function g takes its maximum at $y^+ = y_c^+ = 1/\sqrt{2\eta}$, and y_c^+ represents the height of the controlling vortices where the jet force F_z is maximum [note that in (40), g is normalized by its maximum value $g(y_c^+) = y_c^+\exp(-0.5)$]. The control force depends on three parameters, i.e., the forcing amplitude A, the spanwise wavelength $\Lambda = 2\pi/\beta$, and the control height y_c^+. Note that A can also be scaled in viscous units as $A^+ = A\nu/u_\tau^3$; similarly, $\Lambda^+ = 2\pi/\beta^+ = 2\pi L^+z/\beta$. For $\mathrm{Re}_\tau \approx 200$, the optimal forcing magnitude $A^+ \approx 0.015$, which induces a maximum of $4u_\tau$ spanwise velocity perturbation; the optimal wavelength $\Lambda^+ = 360\pi$ corresponds to a simultaneously control of $\sim$10 near-wall streaks, and $y_c^+ = 30$ targets at the typical height of the buffer layer thickness.

Under SOJF control, the energy equations for the coherent and random parts are, respectively,

$$\epsilon_C = \underbrace{\nu\partial_y\partial_y\frac{\overline{\tilde{u}_i\tilde{u}_i}}{2}}_{D_C}\underbrace{-\partial_y(\overline{\tilde{v}\tilde{u}_i\tilde{u}_i}/2 + \overline{\tilde{u}_i\widetilde{u_i''v''}} + \overline{\tilde{v}\tilde{p}})}_{S_{TC}}\underbrace{-\overline{\tilde{u}\tilde{v}}\partial_y\bar{u}}_{P_{MC}} + \underbrace{\overline{\widetilde{u_i''u_j''}\partial_j\tilde{u}_i}}_{-P_{CR}} + \underbrace{\overline{\tilde{w}\tilde{F}_z}}_{W_C}, \tag{41a}$$

$$\epsilon_R = \underbrace{\nu\partial_y\partial_y\frac{\overline{u_i''u_i''}}{2}}_{D_R}\underbrace{-\partial_y(\overline{u_i''u_i''v''}/2 + \overline{\tilde{v}\widetilde{u_i''u_i''}}/2 + \overline{v''p''})}_{S_{TR}}\underbrace{-\overline{u''v''}\partial_y\bar{u}}_{P_{MR}}\underbrace{-\overline{\widetilde{u_i''u_j''}\partial_j\tilde{u}_i}}_{P_{CR}}. \tag{41b}$$

Similar to SWO, the control power of SOJF is injected through the coherent motion $W_C = \overline{\tilde{w}\tilde{F}_z} = \overline{wF_z}$, and the random power input $W_R = 0$.

Figure 6(a) shows the budget of the coherent kinetic energy distribution. Near the wall ($y^+ < 10$), dissipation balances diffusion, akin to that without control [55]. However, in the buffer layer ($10 < y^+ < 40$), due to the large-scale swirls induced by the SOJF, the spatial transport term overcomes the dissipation term and balances the production (P_{MC}), contrasting the dominant dissipation across the entire flow without control. Moreover, the production term P_{CR} transfers significant amounts of energy from coherent to random motions, a feature not observed in either OBS or SWO controls. The work done by the forcing, as expected, reaches a maximum at around $y^+ = 30$, the location of the wall-jet height. Note that the coherent dissipation shows a monotonic decrease with increasing wall distance. Near the wall, the SOJF leads to the strong spanwise shear of $\partial_y\tilde{w}$, hence generating an intense streamwise vorticity sheet and the largest dissipation at the wall. Further away from the wall, the opposed wall jets collide and induce a strong upward flow motion in the middle span of a channel, leading to large $\partial_z\tilde{v}$ and streamwise vorticity again. Associated with the streamwise vorticity, coherent dissipation shows an intermediate plateau in the buffer layer centered around

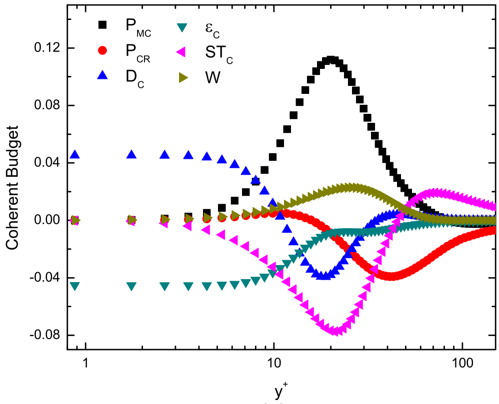

(a)

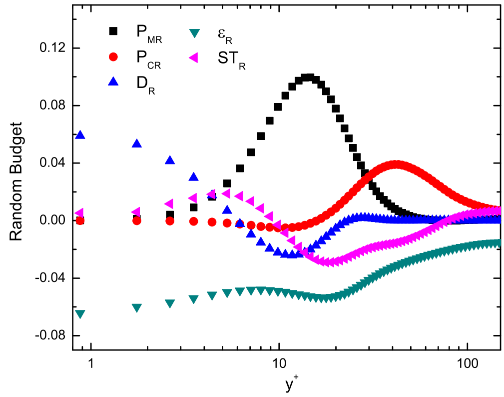

(b)

FIG. 6. Energy budget at $\mathrm{Re}_\tau = 200$ for (a) coherent kinetic energy and (b) random fluctuation kinetic energy under SOJF control.

$y_c^+ = 30$. However, towards the centerline, the large-scale swirls induced by the SOJF are less intense and hence dissipation gradually decreases to zero for $y^+ > 50$.

For the random kinetic energy budget [shown in Fig. 6(b)], the distribution of each term is quite similar to the uncontrolled case near the wall, but a difference emerges above the buffer layer. Note that there are two production terms, one from coherent motion and the other from mean flow. For $y^+ > y_c^+$, production from coherent motions overtakes that from the mean flow, compensating the effects of dissipation and spatial transport. Compared to the mean kinetic energy budget, the random dissipation is overwhelmingly larger than the coherent dissipation. The reason is that under control, there are still a large number of vortical structures surviving in the flow [15]. These vortical structures are concentrated along the middle span of the channel by SOJF and lifted up to the outer flow by the colliding wall jets, inducing intense random turbulent fluctuations and hence large random dissipation. To further validate this point, we examine in the following section the distribution of random dissipation, which coincides well with the locations of vortical structures, all distributed near the middle span of the channel. Therefore, the random vortical structures generate substantial turbulent dissipation—much larger than the coherent dissipation due to the streamwise vortex sheet.

Figure 7 shows the energy fluxes (all the quantities have been normalized by the pumping power of uncontrolled flow at $\mathrm{Re}_\tau \approx 200$). Without control, 59% of the pumping power is dissipated by the mean flow while the remaining 41% by the turbulent dissipation. Under SOJF control, the input pumping power is reduced to 83%, yielding 17% drag reduction. While the mean flow dissipation remains almost unchanged (i.e., 57%), turbulent production decreases remarkably from 49% to 26%, while 11% and 15% go to coherent and random turbulent fields, respectively. Random dissipation drops from 41% to 25%, while coherent dissipation only consumes 3% of the pumping power. Compared to SWO, the power input W_c for SOJF is much smaller, viz., only 2%, indicating a 15% net power saving. Although the power saving is slightly smaller than that of OBS, the SOJF injects energy through coherent large-scale swirls, hence independent of instantaneous flow sensing and actuation.

D. Comparison of different control methods

Pursuant to Eqs. (32) and (30), the bar chart for different components of drag reduction and the net power saving rate in terms of $\mathcal{N}_M, \mathcal{N}_R, \mathcal{N}_C$, and $\mathcal{N}_{\mathrm{in}}$ are presented in Fig. 8. As mentioned earlier herein, although all controls result in approximately 20% drag reduction, SWO control requires the largest energy input, followed by the SOJF and the OBS controls. While the SWO controls both

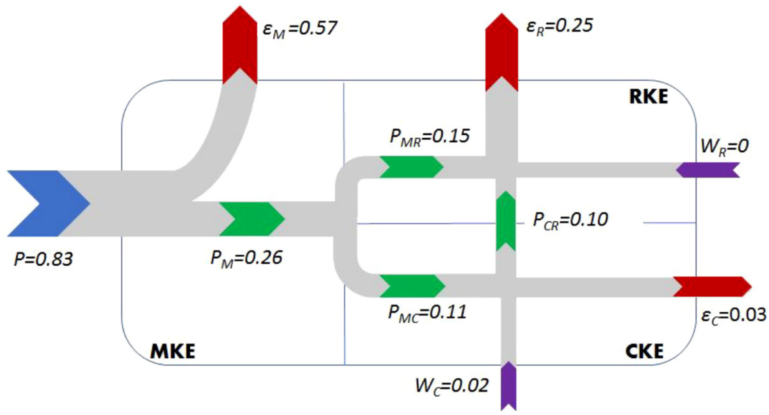

FIG. 7. Energy flux in turbulent channel under SOJF for $\mathrm{Re}_\tau = 200$.

mean flow ($\mathcal{N}_M = 11\%$) and random turbulence ($\mathcal{N}_R = 12\%$) dissipation notably, OBS ($\mathcal{N}_R = 14\%$) and SOJF ($\mathcal{N}_R = 16\%$) are effective in reducing the random turbulence dissipation only, which is due to the direct suppression of random vortical motions.

Comparisons of different control methods are also made for the wall-normal distributions of dissipation, shown in Fig. 9. Note that all the dissipation in this figure is normalized by the uncontrolled pumping power such that $\mathcal{N} = 1 - \int_0^1 (|\epsilon_M| + |\epsilon_R| + |\epsilon_C|)dy$ according to Eq. (30). For the mean dissipation [Fig. 9(a)], its value at the wall is actually u_τ^4/ν, whose difference from the uncontrolled case represents the change of drag coefficient—all the three controls yield about 20% drag reduction. Both SOJF and OBS controls have a larger mean dissipation for $y \gtrsim 0.04$ (for $y^+ \gtrsim 10$) than the uncontrolled case, due to the induced ejecting motions transporting low momentum fluids to flow regions further away from the wall (causing higher shear and hence larger dissipation). For the random turbulent dissipation [Fig. 9(b)], all the controls suppress it notably throughout the entire wall-normal location, except for OBS showing a larger dissipation at the wall due to random blowing and suction motions. For the coherent dissipation [Fig. 9(c)], SWO induces a much larger dissipation than SOJF control, hence no net power saving.

Based on the above comparison, it would be interesting to use a hybrid control method combining OBS and SOJF so that control power is injected through both coherent and random turbulent

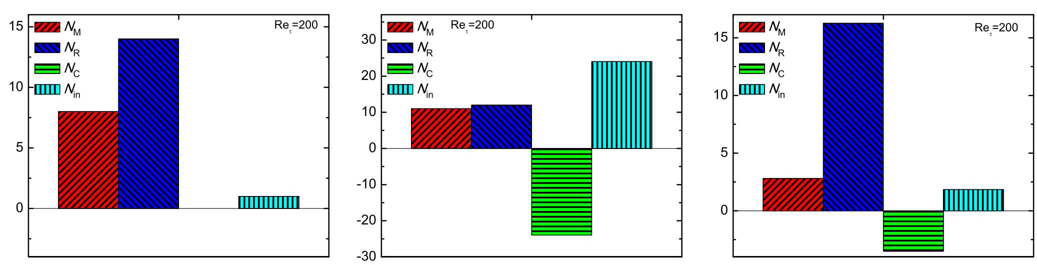

(a) (b) (c)

FIG. 8. Bar chart of drag reduction rate by $\mathcal{N}_M$, suppression of dissipation of mean flow, $\mathcal{N}_R$, suppression of random turbulent dissipation, $\mathcal{N}_C$, coherent dissipation induced by control, and $\mathcal{N}_{\mathrm{in}}$, power input by control, for (a) OBS, (b) SWO, and (c) SOJF control; all at $\mathrm{Re}_\tau = 200$. Note that OBS control involves zero coherent dissipation as the energy is injected to the flow through random turbulence fluctuation.

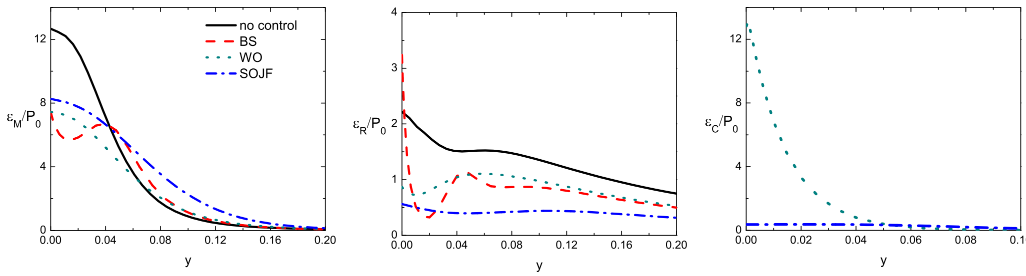

FIG. 9. Profiles of mean dissipation, random turbulent dissipation, and coherent dissipation (all normalized by the pumping power P_0) for channels at $\mathrm{Re}_\tau \approx 200$ with OBS control (dashed line), SWO control (dotted line), SOJF control (dashed-dotted line), and no control (solid line).

motions. This way, a higher drag reduction and net power saving may be achieved. Moreover, how to control the mean flow more effectively with less energy remains a challenge.

IV. DISCUSSION

A. Random dissipation and its relationship to vortical structures

Note that Eq. (16) expresses C_f in terms of triple-decomposed dissipation, which can be further linked to different flow structures as follows. In all these controls, the mean dissipation is a direct consequence of the spanwise mean vorticity $\Omega_z = \partial_y U$, which corresponds to the sheetlike structure of the mean flow; the coherent dissipation is mainly from the streamwise vorticity Ω_x, due to the wall-jet and the large-scale swirls of SOJF, or the Stokes layer induced by SWO. Both the mean and coherent dissipations are maximum at the wall due to the strongest shear at the wall. The remaining question is what structures are responsible for the random dissipation. Below, we take SOJF control as an example, to show that it is the remnant vortical structures which generate the turbulent fluctuations and hence cause random dissipation under control.

Figure 10 (left) shows the isocontours of ϵ_R in the flow under SOJF control, remarkably, all concentrated near the middle span of the channel. Recalling the delineation in Yao *et al.* [15], near-wall streaks are pressed together to form fewer, unstable streaks with high flank angles. These streaks generate a cluster of vortical structures through the streaks' instability or transient growth, lying also along the middle span. As a result, these vortical structures induce intense turbulence fluctuations, hence yielding high dissipation along the center of the channel. In Fig. 10 (right), we plot the isocontours of λ_2 vortices [56]. Furthermore, to show that the ϵ_R and λ_2 structures are colocated, we take two cross sections at $x/L_x = 1/3$ and $5/8$. It is clear that the vortical structures are predominately tubelike with dissipation structures at their periphery (where the strain rate is maximized, but minimized at the core)—akin to the finding by Refs. [57,58]—suggesting that the random dissipation is mainly caused by the vortical structures.

B. Reynolds number effects

To demonstrate how different dissipation components vary with increasing Re, we choose SWO control at a higher $\mathrm{Re}_\tau = 2000$ as an example. Our recent study [10] has shown that $\mathcal{R} = 22\%$ drag reduction can be achieved at $\mathrm{Re}_\tau = 2000$ with $A^+ = 12$ and $T^+ = 100$. Note that simulations for SOJF and OBS controls at comparable $\mathrm{Re}_\tau = 2000$ were not performed due to the computation cost as well as the difficulty in determining the optimal control parameters.

The triple-decomposed energy box at $\mathrm{Re}_\tau = 2000$ is shown in Fig. 11. Without control, about 40% of pumping power is dissipated by the mean flow, while 60% by the turbulent dissipation—much higher than the case at $\mathrm{Re}_\tau = 200$ where turbulent dissipation takes only 40% of pumping

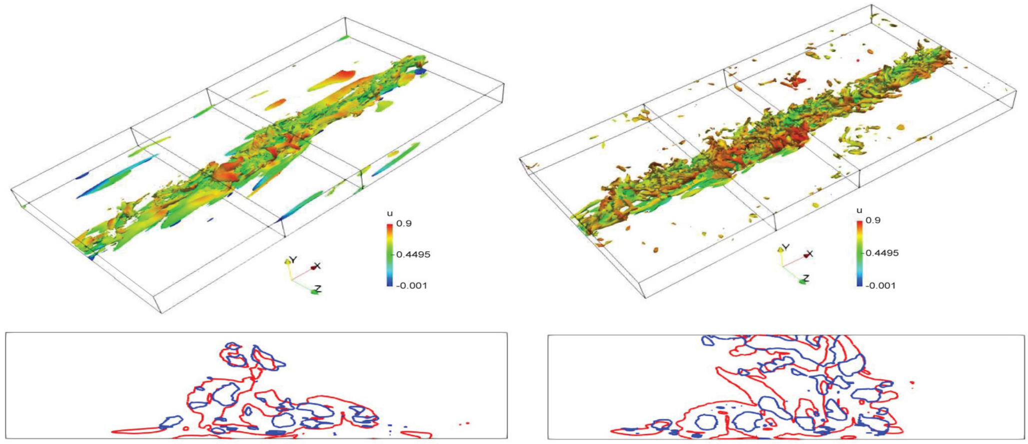

FIG. 10. Distribution of random turbulent dissipation under SOJF control at $\mathrm{Re}_\tau = 180$. Top left: Isosurface of random turbulent dissipation ($\epsilon_R = 1.5 \times 10^{-3}$) colored by u. Top right: Isosurface of λ_2 structure ($\lambda_2 = -0.35$) colored by u. Bottom left and right: Contours of ϵ_R (red lines) and λ_2 (blue lines) at the cross planes $x/L_x = 1/3$ and $5/8$, respectively. The two cross planes are marked in both top panels.

power. Under control, the input pumping power is reduced to 78%, yielding a 22% drag reduction at $\mathrm{Re}_\tau = 2000$, smaller than 35% drag reduction at $\mathrm{Re}_\tau = 200$ with the same $A^+ = 12$. However, the coherent dissipation decreases from 79% to 56%, leading to a notable reduction of input power (by about 23%) at $\mathrm{Re}_\tau = 2000$. At $\mathrm{Re}_\tau = 200$, the mean dissipation is suppressed by 15%, while at $\mathrm{Re}_\tau = 2000$ the mean dissipation only decreases by 4% (from 40% to 36%). Moreover, ϵ_R increases from 21% at $\mathrm{Re}_\tau = 200$ to 43% at $\mathrm{Re}_\tau = 2000$, indicating that more energy is dissipated by the random turbulence. Again, the coherent and random energy fluxes are nearly decoupled—only 1% of the pumping power is transferred from coherent to random fluctuations. This is because even at this high Re the coherent velocity field is essentially the Stokes layer solution, so that viscous diffusion almost balances the dissipation pursuant to Eq. (39); hence so small an amount of energy is transferred to a random field.

From the discussion above, it is clear that random turbulent dissipation has the dominant contribution to C_f at high Re; hence it is increasingly important to suppress these dissipation structures as displayed in Fig. 10. Based on our previous studies [10,15], under control there are still numerous small-scale vortical structures remaining in the flow, whose number/intensity

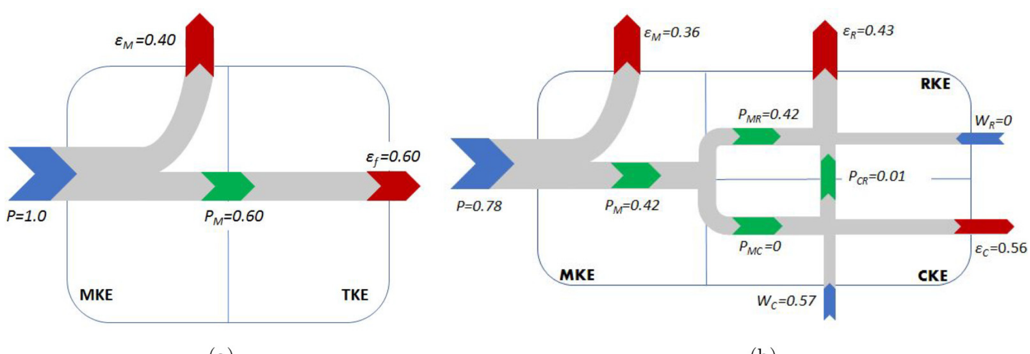

FIG. 11. Energy flux for (a) without control and (b) under SWO control at $\mathrm{Re}_\tau = 2000$.

continuously increases with Re. Hence, the elimination of those structures is a great challenge for drag reduction at high Re. As explained earlier, though dissipation is induced by the viscous strain of fluids at the smallest (Kolmogorov) scale, there is no indication that small-scale control should be dominant over large-scale control, as suppressing large-scale turbulence would intercept the energy cascade, hence leading to smaller ϵ_R and therefore reducing drag. This means that control of large- or very-large-scale motions [59,60] is as valuable as previous ideas on intercepting the regeneration of near-wall small-scale vortices [61], and a hybrid control of both small- and large-scale turbulence seems to be promising (e.g., through a combination of OBS and SOJF).

V. CONCLUSION

A comparative examination of the wall friction drag reduction efficacy for different control methods (e.g., SOJF, SWO, and OBS) is presented. It is built on a different approach of a friction coefficient using a triple-decomposed energy flux. Differing from the FIK or the RD identity, the drag coefficient is expressed in terms of the volume integrated dissipation and the forcing energy by external excitations. Compared to the energy-box analysis by Gatti *et al.* [21], our study here uncovers how controls of mean flow, coherent flow, and random turbulence contribute differently to the drag reduction and the net power saving. It shows that while vortex sheets of Ω_z and Ω_x contribute to mean and coherent dissipations, respectively, λ_2 vortex structures generating random turbulent fluctuations and hence random dissipation are the dominant contributors to the drag at high Re. We establish that suppression of the near-wall vortical structures remains the clear target for the successful control at high Re, and a promising perspective may be a hybrid control strategy by incorporating different methods to achieve drag reduction and net power saving at high Re. Compared to the FIK and RD identities, our diagnosis of Eq. (3) focuses on the spatially homogenous flow and can be similarly extended to analyze compressible effects [47,62–64]. For spatially developing flows (e.g., turbulent boundary layer), there should be an additional term in Eq. (3) characterizing energy transport in the flow direction, whose explicit expression may vary with boundary conditions (e.g., pressure gradient, wall curvature, roughness, etc.).

ACKNOWLEDGMENTS

This work is partially supported by Research Projects No. 12072012 (National Natural Science Foundation of China), No. 11721202 (National Natural Science Foundation of China), and No. 91952302 (National Natural Science Foundation of China), and the President's Distinguished Chair funds of Texas Tech University. Computational resources provided by Beihang University (High Performance Computing Platform), Texas Tech University (HPCC), TACC Lonestar are acknowledged.

---

[1] A. G. Kravchenko, H. Choi, and P. Moin, On the relation of near-wall streamwise vortices to wall skin friction in turbulent boundary layers, Phys. Fluids A **5**, 3307 (1993).

[2] J. Jiménez and A. Pinelli, The autonomous cycle of near-wall turbulence, J. Fluid Mech. **389**, 335 (1999).

[3] F. Waleffe, On a self-sustaining process in shear flows, Phys. Fluids **9**, 883 (1997).

[4] B.-Q. Deng, C.-X. Xu, W.-X. Huang, and G.-X. Cui, Strengthened opposition control for skin-friction reduction in wall-bounded turbulent flows, J. Turbul. **15**, 122 (2014).

[5] N. Kasagi, Y. Suzuki, and K. Fukagata, Microelectromechanical systems-based feedback control of turbulence for skin friction reduction, Annu. Rev. Fluid Mech. **41**, 231 (2009).

[6] W. Jung, N. Mangiavacchi, and R. Akhavan, Suppression of turbulence in wall-bounded flows by high-frequency spanwise oscillations, Phys. Fluids A **4**, 1605 (1992).

[7] J.-I. Choi, C.-X. Xu, and H. J. Sung, Drag reduction by spanwise wall oscillation in wall-bounded turbulent flows, AIAA J. **40**, 842 (2002).

[8] P. Ricco and M. Quadrio, Wall-oscillation conditions for drag reduction in turbulent channel flow, Int. J. Heat Fluid Flow **29**, 891 (2008).
[9] L. Agostini, E. Touber, and M. A. Leschziner, Spanwise oscillatory wall motion in channel flow: drag-reduction mechanisms inferred from dns-predicted phase-wise property variations at Re = 1000, J. Fluid Mech. **743**, 606 (2014).
[10] J. Yao, X. Chen, and F. Hussain, Reynolds number effect on drag control via spanwise wall oscillation in turbulent channel flows, Phys. Fluids **31**, 085108 (2019).
[11] H. Choi, P. Moin, and J. Kim, Active turbulence control for drag reduction in wall-bounded flows, J. Fluid Mech. **262**, 75 (1994).
[12] Y. M. Chung and T. Talha, Effectiveness of active flow control for turbulent skin friction drag reduction, Phys. Fluids **23**, 025102 (2011).
[13] B.-Q. Deng and C.-X. Xu, Influence of active control on stg-based generation of streamwise vortices in near-wall turbulence, J. Fluid Mech. **710**, 234 (2012).
[14] H. Mamori, K. Iwamoto, and A. Murata, Effect of the parameters of traveling waves created by blowing and suction on the relaminarization phenomena in fully developed turbulent channel flow, Phys. Fluids **26**, 015101 (2014).
[15] J. Yao, X. Chen, and F. Hussain, Drag control in wall-bounded turbulent flows via spanwise opposed wall-jet forcing, J. Fluid Mech. **852**, 678 (2018).
[16] T. C. Corke and F. O. Thomas, Active and passive turbulent boundary-layer drag reduction, AIAA J. **56**, 3835 (2018).
[17] J. M. Hamilton, J. Kim, and F. Waleffe, Regeneration mechanisms of near-wall turbulence structures, J. Fluid Mech. **287**, 317 (1995).
[18] W. Schoppa and F. Hussain, Coherent structure generation in near-wall turbulence, J. Fluid Mech. **453**, 57 (2002).
[19] K. Fukagata, K. Iwamoto, and N. Kasagi, Contribution of reynolds stress distribution to the skin friction in wall-bounded flows, Phys. Fluids **14**, L73 (2002).
[20] N. Renard and S. Deck, A theoretical decomposition of mean skin friction generation into physical phenomena across the boundary layer, J. Fluid Mech. **790**, 339 (2016).
[21] D. Gatti, A. Cimarelli, Y. Hasegawa, B. Frohnapfel, and M. Quadrio, Global energy fluxes in turbulent channels with flow control, J. Fluid Mech. **857**, 345 (2018).
[22] M. de Giovanetti, Y. Hwang, and H. Choi, Skin-friction generation by attached eddies in turbulent channel flow, J. Fluid Mech. **808**, 511 (2016).
[23] S. Deck, N. Renard, R. Laraufie, and P.-E. Weiss, Large-scale contribution to mean wall shear stress in high-Reynolds-number flat-plate boundary layers up to Re = 13650, J. Fluid Mech. **743**, 202 (2014).
[24] E. Hurst, Q. Yang, and Y. M. Chung, The effect of reynolds number on turbulent drag reduction by streamwise travelling waves, J. Fluid Mech. **759**, 28 (2014).
[25] Y.-S. Wang, W.-X. Huang, and C.-X. Xu, Active control for drag reduction in turbulent channel flow: the opposition control schemes revisited, Fluid Dyn. Res. **48**, 055501 (2016).
[26] L. Agostini and M. Leschziner, The impact of footprints of large-scale outer structures on the near-wall layer in the presence of drag-reducing spanwise wall motion, Flow, Turbul. Combust. **100**, 1037 (2018).
[27] J. C. Vassilicos, Dissipation in turbulent flows, Annu. Rev. Fluid Mech. **47**, 95 (2015).
[28] F. Laadhari, Reynolds number effect on the dissipation function in wall-bounded flows, Phys. Fluids **19**, 038101 (2007).
[29] H. Abe and R. A. Antonia, Relationship between the energy dissipation function and the skin friction law in a turbulent channel flow, J. Fluid Mech. **798**, 140 (2016).
[30] A. K. M. F. Hussain, Coherent structures – reality and myth, Phys. Fluids **26**, 2816 (1983).
[31] T. Wei, Integral properties of turbulent-kinetic-energy production and dissipation in turbulent wall-bounded flows, J. Fluid Mech. **854**, 449 (2018).
[32] W. Reynolds and A. Hussain, The mechanics of an organized wave in turbulent shear flow. part 3. theoretical models and comparisons with experiments, J. Fluid Mech. **54**, 263 (1972).
[33] S. Laizet and E. Lamballais, High-order compact schemes for incompressible flows: A simple and efficient method with quasi-spectral accuracy, J. Comput. Phys. **228**, 5989 (2009).

[34] S. Laizet and N. Li, Incompact3d: A powerful tool to tackle turbulence problems with up to o (105) computational cores, Int. J. Numer. Methods Fluids **67**, 1735 (2011).
[35] M. Lee and R. D. Moser, Direct numerical simulation of turbulent channel flow up to re 5200, J. Fluid Mech. **774**, 395 (2015).
[36] J. Kim, P. Moin, and R. Moser, Turbulence statistics in fully developed channel flow at low reynolds number, J. Fluid Mech. **177**, 133 (1987).
[37] E. Hammond, T. Bewley, and P. Moin, Observed mechanisms for turbulence attenuation and enhancement in opposition controlled wall-bounded flows, Phys. Fluids **10**, 2421 (1998).
[38] Q.-J. Xia, W.-X. Huang, C.-X. Xu, and G.-X. Cui, Direct numerical simulation of spatially developing turbulent boundary layers with opposition control, Fluid Dyn. Res. **47**, 025503 (2015).
[39] A. Stroh, B. Frohnapfel, P. Schlatter, and Y. Hasegawa, A comparison of opposition control in turbulent boundary layer and turbulent channel flow, Phys. Fluids **27**, 075101 (2015).
[40] M. Quadrio and P. Ricco, Critical assessment of turbulent drag reduction through spanwise wall oscillations, J. Fluid Mech. **521**, 251 (2004).
[41] E. Touber and M. A. Leschziner, Near-wall streak modification by spanwise oscillatory wall motion and drag-reduction mechanisms, J. Fluid Mech. **693**, 150 (2012).
[42] P. Orlandi and M. Fatica, Direct simulations of turbulent flow in a pipe rotating about its axis, J. Fluid Mech. **343**, 43 (1997).
[43] M. Quadrio and S. Sibilla, Numerical simulation of turbulent flow in a pipe oscillating around its axis, J. Fluid Mech. **424**, 217 (2000).
[44] I. Yudhistira and M. Skote, Direct numerical simulation of a turbulent boundary layer over an oscillating wall, J. Turbul. **12**, N9 (2011).
[45] M. Skote, Temporal and spatial transients in turbulent boundary layer flow over an oscillating wall, Int. J. Heat Fluid Flow **38**, 1 (2012).
[46] M. P. Hack and T. A. Zaki, The influence of harmonic wall motion on transitional boundary layers, J. Fluid Mech. **760**, 63 (2014).
[47] M. Skote, M. Mishra, and Y. Wu, Wall oscillation induced drag reduction zone in a turbulent boundary layer, Flow Turbul. Combust. **102**, 641 (2019).
[48] S. Straub, R. Vinuesa, P. Schlatter, B. Frohnapfel, and D. Gatti, Turbulent duct flow controlled with spanwise wall oscillations, Flow, Turbul. Combust. **99**, 787 (2017).
[49] J. Yao, X. Chen, F. Thomas, and F. Hussain, Large-scale control strategy for drag reduction in turbulent channel flows, Phys. Rev. Fluids **2**, 062601 (2017).
[50] W. Schoppa and F. Hussain, A large-scale control strategy for drag reduction in turbulent boundary layers, Phys. Fluids **10**, 1049 (1998).
[51] G. Iuso, M. Onorato, P. G. Spazzini, and G. M. di Cicca, Wall turbulence manipulation by large-scale streamwise vortices, J. Fluid Mech. **473**, 23 (2002).
[52] J. Canton, R. Örlü, C. Chin, and P. Schlatter, Reynolds number dependence of large-scale friction control in turbulent channel flow, Phys. Rev. Fluids **1**, 081501 (2016).
[53] A. R. Hoskinson, N. Hershkowitz, and D. E. Ashpis, Force measurements of single and double barrier dbd plasma actuators in quiescent air, J. Phys. D **41**, 245209 (2008).
[54] M. Wicks, F. O. Thomas, T. C. Corke, M. Patel, and A. B. Cain, Mechanism of vorticity generation in plasma streamwise vortex generators, AIAA J. **53**, 3404 (2015).
[55] X. Chen, F. Hussain, and Z. She, Quantifying wall turbulence via a symmetry approach: Part II. Reynolds stresses, J. Fluid Mech. **850**, 401 (2018).
[56] J. Jeong and F. Hussain, On the identification of a vortex, J. Fluid Mech. **285**, 69 (1995).
[57] I. Bermejo-Moreno, D. Pullin, and K. Horiuti, Geometry of enstrophy and dissipation, grid resolution effects and proximity issues in turbulence, J. Fluid Mech. **620**, 121 (2009).
[58] J. Yao and F. Hussain, A physical model of turbulence cascade via vortex reconnection sequence and avalanche, J. Fluid Mech. **883**, A51 (2020).
[59] I. Marusic, R. Mathis, and N. Hutchins, Predictive model for wall-bounded turbulent flow, Science **329**, 193 (2010).

[60] L. H. Hellström, I. Marusic, and A. J. Smits, Self-similarity of the large-scale motions in turbulent pipe flow, J. Fluid Mech. **792**, R1 (2016).
[61] K. Iwamoto, K. Fukagata, N. Kasagi, and Y. Suzuki, Friction drag reduction achievable by near-wall turbulence manipulation at high Reynolds numbers, Phys. Fluids **17**, 011702 (2005).
[62] T. Gomez, V. Flutet, and P. Sagaut, Contribution of reynolds stress distribution to the skin friction in compressible turbulent channel flows, Phys. Rev. E **79**, 035301(R) (2009).
[63] J. Yao and F. Hussain, Supersonic turbulent boundary layer drag control using spanwise wall oscillation, J. Fluid Mech. **880**, 388 (2019).
[64] W. Li, Y. Fan, D. Modesti, and C. Cheng, Decomposition of the mean skin-friction drag in compressible turbulent channel flows, J. Fluid Mech. **875**, 101 (2019).